RESEARCH ARTICLE

Gearing for speed slows the predatory strike of a mantis shrimp

Matthew J. McHenry[1,*], Thomas Claverie[2], Michael V. Rosario[2] and S. N. Patek[2]

[1]Department of Ecology and Evolution, 321 Steinhaus Hall, University of California, Irvine, CA 92697-2525, USA and [2]Biology Department and Organismic and Evolutionary Biology Graduate Program, University of Massachusetts, Amherst, MA 01003, USA

*Author for correspondence (mmchenry@uci.edu)

SUMMARY

The geometry of an animal's skeleton governs the transmission of force to its appendages. Joints and rigid elements that create a relatively large output displacement per unit input displacement have been considered to be geared for speed, but the relationship between skeletal geometry and speed is largely untested. The present study explored this subject with experiments and mathematical modeling to evaluate how morphological differences in the raptorial appendage of a mantis shrimp (*Gonodactylus smithii*) affect the speed of its predatory strike. Based on morphological measurements and material testing, we computationally simulated the transmission of the stored elastic energy that powers a strike and the drag that resists this motion. After verifying the model's predictions against measurements of strike impulse, we conducted a series of simulations that varied the linkage geometry, but were provided with a fixed amount of stored elastic energy. We found that a skeletal geometry that creates a large output displacement achieves a slower maximum speed of rotation than a low-displacement system. This is because a large displacement by the appendage causes a relatively large proportion of its elastic energy to be lost to the generation of drag. Therefore, the efficiency of transmission from elastic to kinetic energy mediates the relationship between the geometry and the speed of a skeleton. We propose that transmission efficiency plays a similar role in form–function relationships for skeletal systems in a diversity of animals.

Key words: predation, movement, feeding, Crustacea, kinematic transmission, four-bar linkage.

INTRODUCTION

There is a long-standing practice of inferring the mechanical performance of an animal from the geometry of its skeleton. A skeletal geometry that produces a relatively large output displacement per unit input displacement is traditionally considered to be well suited to high-speed motion (Gregory, 1912; Smith and Savage, 1956; Hildebrand, 1974). However, it is largely untested whether this gearing for speed actually produces faster motion under biologically realistic forces. Therefore, we investigated the relationship between skeletal morphology and speed in an exceptionally fast biomechanical system: the predatory strike by the raptorial appendage of the mantis shrimp *Gonodactylus smithii* (Crustacea, Stomatopoda; Fig. 1A).

The gearing provided by a skeleton is most clear in a simple lever. Force acting on a lever is generated by muscular contraction or the release of energy by an elastic structure. The force created by such an actuator is amplified by the mechanical advantage of the lever, which is equal to the ratio of in-lever to out-lever lengths. The mechanical advantage is inversely proportional to the displacement advantage, which is the ratio of output to input displacement. This inverse relationship provides the argument that a lever possesses a trade-off between force and speed that is inherent to its geometry (Gregory, 1912), which we will henceforth refer to as the gearing-for-speed hypothesis. This hypothesis predicts that species possessing a relatively high displacement advantage will move faster than related species with a low displacement advantage.

In the past century, the gearing-for-speed hypothesis has been used to interpret the potential for fast motion in species with a variety of skeletal lever systems. A classic example is the leg bones of mammals, where the limbs joints of a horse have a higher

displacement advantage than a slow-moving armadillo (Smith and Savage, 1956). This practice of using displacement advantage as an index of speed carries through to the contemporary literature. For example, recent studies have inferred the bite speed of extinct dinosaurs from displacement advantage (Barrett and Reyfeld, 2006; Sakamoto, 2010). Such interpretations have been extended beyond simple lever systems. For example, the ability of some muscular hydrostats, such as squid tentacles and lizard tongues, to perform a rapid predatory strike has been attributed to a high displacement advantage (Kier and Smith, 1985). The same argument has been offered for four-bar linkage systems, which are composed of four rigid skeletal elements (i.e. links) that are connected together by four joints (Paul, 1979). The displacement advantage of a linkage system is defined by its kinematic transmission, T_k, which is the ratio of output rotation to input rotation (Anker, 1974; Muller, 1987). As for a linear measure of displacement advantage, a high T_k has been interpreted as facilitating rapid motion (Muller, 1987; Westneat, 1995). In support of this view, fish species that feed on evasive prey have higher values of T_k than related species that feed on slow-moving prey (Westneat, 1995; Wainwright et al., 2004).

Models that consider the dynamic forces of lever systems offer a more complex view of the relationship between the geometry and the speed of a skeleton. The gearing-for-speed hypothesis holds true in cases where an actuator contracts at a fixed rate, irrespective of the load it encounters. Under such conditions, the linear output speed of a system will be proportional to its displacement advantage. However, both elastic actuators and muscles generally shorten more slowly when resisted by a greater load, and such resistance may depend on the lever's geometry. For example, the leg muscles of the frog *Xenopus laevis* shorten more slowly when they actuate a lever system with a

higher displacement advantage, due to the force–velocity relationship that is intrinsic to muscle (Richards, 2011). Therefore, the speed gains of a high displacement advantage may be offset by a slower rate of shortening by the actuator. To account for how a force transmission system may affect both actuators and loads, forward dynamic models can predict the speed of motion from a consideration of mechanics (Zajac, 1993; Daniel, 1995). The present study has adopted the use of such modeling to examine how speed varies across changes in leverage when the input energy remains fixed.

The predatory strike of a mantis shrimp is powered by elastic energy stored within its exoskeleton. This energy is generated by a lateral extensor muscle that adducts a V-shaped element (the meral-V; Fig. 1B) at the distal end of the merus segment of the second thoracic appendages, known as the 'raptorial appendages'. The strike begins when the meral-V is released by a latch mechanism at the start of a strike (Burrows, 1969; Patek et al., 2004; Patek et al., 2007; Zack et al., 2009). During the strike, the merus functions as a spring through the abduction of the meral-V, a mechanism that we will henceforth refer to as the 'meral spring'. Mantis shrimp transmit the force for a predatory strike with a four-bar linkage (Fig. 1A–C) (Patek et al., 2007). The meral spring engages the four-bar linkage (Fig. 1C) (Patek et al., 2007), which is rigidly coupled to distal segments that consequently swing away from the merus to strike a prey. These segments (the carpus, propodus and dactyl; Fig. 1B) rotate as a uniform rigid mass, the striking body, to impact the prey. The mass of the striking body and the fluid forces it generates serve to resist the action of the meral spring to power the strike.

The present study considered the interacting dynamics of the meral spring, the striking body and four-bar linkage to determine how the rotation speed of a strike depends on the morphology of the raptorial appendage. This was achieved by developing a mathematical model of these dynamics and performing a series of experimental measurements to characterize the system. We tested the model by comparing its prediction of strike impulse with measurements. Once verified, the model provided the basis for exploring how morphological differences affect strike speed.

MATERIALS AND METHODS

Our mathematical model required a variety of experimental techniques to comprehensively characterize the mechanics of a raptorial appendage. To calculate the torque generated by the meral spring during a strike (τ_{spring}; Fig. 1D), we measured its stiffness by materials testing. Measurements of the linkage lengths and the angle of the meral spring were used to calculate the gearing of the four-bar linkage over the course of a strike (Fig. 1C). According to our model, the torque applied to the striking body ($\tau_{applied}$) is inversely proportional to the T_k of the four-bar linkage ($T_k=d\theta/d\gamma$, where θ and γ are the output and input angles, respectively; Fig. 1C) and is resisted by the moment of inertia of the striking body and the drag generated by the surrounding water (Fig. 1D). We modeled the drag force from morphometrics of the striking body and measured the moment of inertia using density and shape information from micro-computed tomography (CT). Once verified with strike impulse measurements, a series of simulations were conducted to evaluate how differences in the meral spring, four-bar linkage and striking body affect the rotation speed of a strike.

Mathematical model
Linkage geometry

The geometry of the four-bar linkage system was measured from the coordinates of each joint [as in Patek et al. (Patek et al., 2007)]. These coordinates were defined within a two-dimensional Cartesian
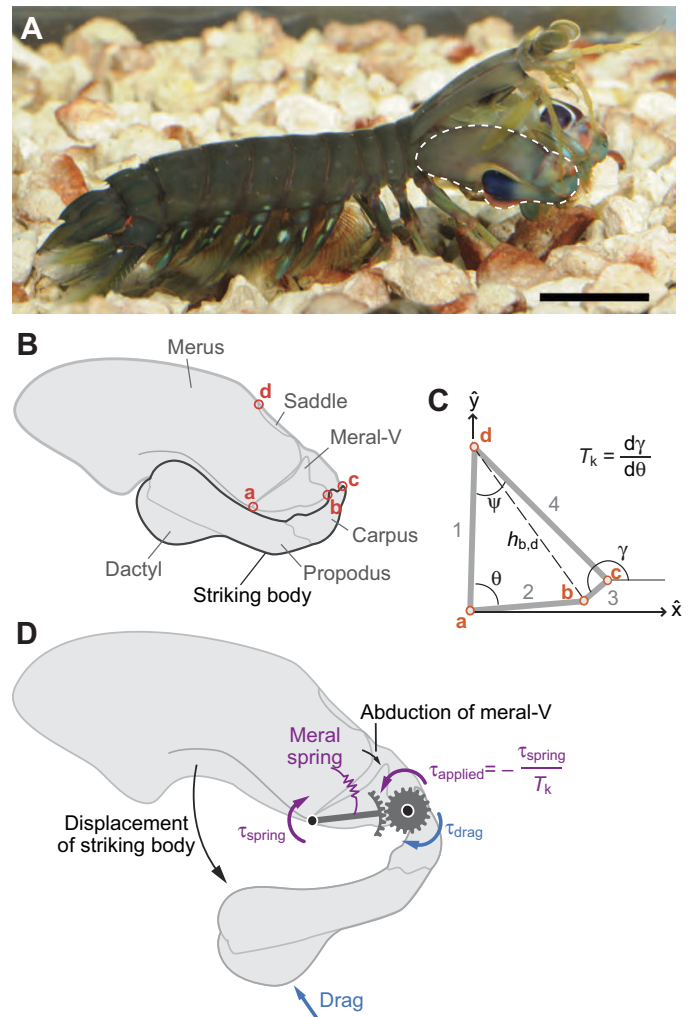

Fig. 1. The raptorial appendage of the mantis shrimp. (A) *Gonodactylus smithii* uses its raptorial appendage (dashed outline) to capture and process prey. Scale bar, 2 cm. (B) A schematic of the raptorial appendage in a loaded position (meral-V rotated proximally), with its major anatomical features labeled. The striking body is composed of the carpus, the propodus and the dactyl (black outline), which moves as a single rigid structure during a strike. Joints in the merus, meral-V and carpus (denoted as **a–d**, with orange circles) define the geometry of the four-bar linkage system that gears the meral spring to the striking body. (C) The geometry of the linkage system was used to calculate the kinematic transmission (T_k), as a function of the input angle, θ. (D) A schematic illustration of our mathematical model illustrates how the torque generated by the meral spring (τ_{spring}, Eqn 5) is geared by the linkage system to generate torque that is applied to the striking body ($\tau_{applied}$, Eqn 6). This force transmission system was modeled with gearing that varied with the input angle, as dictated by the T_k of the linkage system (Patek et al., 2007). The motion of the striking body was modeled as pure rotation about point **b**. We modeled the resistance to the spring torque arising from the mass of the striking body and drag (straight blue arrow), which created a resistive torque (τ_{drag}, Eqn 7). Additional symbol definitions are provided in the List of symbols and are described in the Materials and methods.

coordinate system with the unit vectors $\hat{x}$ and $\hat{y}$ and an origin, **a**, that was fixed to the merus and denoted the pivot point for the meral-V (Fig. 1B,C). The joint **d** was also fixed to the merus and defined the direction of $\hat{y}$. Joints **b** and **c** moved relative to the merus, but maintained fixed distances from adjacent points over the course of a strike because of the rigidity of skeletal elements in each link.

The angle between links 1 and 2 served as the input angle (θ) to the linkage system, which increased in value over the course of a strike as the meral-V rotated away from the merus. All angles were recorded in radians for our calculations, but were presented in degrees to conform with the convention in the literature. The input angle between the meral-V and the carpus determined the coordinates of joint **b**, as follows:

$$\mathbf{b} = l_2 \sin(\theta)\hat{\mathbf{x}} + l_2 \cos(\theta)\hat{\mathbf{y}} , \qquad (1)$$

where l_2 is the length of link 2 (Fig. 1C). The distance between **b** and **d** ($h_{b,d}$) was useful for defining the rest of the linkage system and was calculated as follows:

$$h_{b,d} = \sqrt{l_1^2 + l_2^2 - 2l_1 l_2 \cos(\theta)} , \qquad (2)$$

where l_1 is the length of link 1. The geometry of a four-bar linkage requires that this distance occurs within bounds defined by the following inequalities: $h_{b,d} < l_3 + l_4$, $h_{b,d} > |l_4 - l_3|$, $h_{b,d} < l_1 + l_2$, and $h_{b,d} > |l_1 - l_2|$, where l_3 and l_4 are the lengths of links 3 and 4, respectively. The distance $h_{b,d}$ factors into the calculation of the angle between links 1 and 4 (ψ) and the position of the second carpus joint (point **c**) (Fig. 1C):

$$\psi = \cos^{-1}\left(\frac{h_{b,d}^2 + l_1^2 - l_2^2}{2h_{b,d}l_1}\right) + \cos^{-1}\left(\frac{h_{b,d}^2 + l_4^2 - l_3^2}{2h_{b,d}l_4}\right) , \qquad (3)$$

$$\mathbf{c} = l_4 \sin(\psi)\hat{\mathbf{x}} + (l_1 - l_4) \cos(\psi)\hat{\mathbf{y}} . \qquad (4)$$

Using these geometric definitions, we calculated the T_k of the linkage systems computationally. The output angle, γ, was defined as the angle of link 3, about joint **c** and relative to the x-axis (Fig. 1C). We calculated values for γ from coordinates **b** (Eqn 1) and **c** (Eqn 4) for 1000 values of θ over the entire range allowed by the above-mentioned inequalities for $h_{b,d}$. Cubic splines were fit to the numerical values of these angles in order to find the continuous functions $\gamma(\theta)$ and $\theta(\gamma)$, which were used in our simulations (described below). T_k was calculated as the first derivative of the output angle function [$T_k(\theta) = \gamma'(\theta)$]. We used the minimum value of T_k ($T_{k,min}$) to provide a single value to characterize a particular geometry. An alternative to our numerical approach would have been to calculate $\gamma(\theta)$ analytically, which requires a series of large equations that do not offer a more elegant expression than our computational method. All analyses and modeling for the present study were performed with scripted programs within MATLAB (R2009a, MathWorks, Natick, MA, USA), unless mentioned otherwise.

Strike dynamics

The torque created by the meral spring functions to abduct the meral-V. We modeled this torque with the following equation:

$$\tau_{spring} = k_{torsion}(\theta - \theta_{rest}) , \qquad (5)$$

where $k_{torsion}$ is the stiffness of the torsion spring ($N\,m\,deg^{-1}$) and θ_{rest} is the resting angle for the spring, which we measured from photographs of the appendage at rest (described below). The meral-V is a flexible strip of exoskeleton that extends when it is released during a strike and maintains a fixed position when at rest (Patek et al., 2007). The torque created by the meral spring is applied to the striking body to a degree that depends on the instantaneous T_k of the four-bar linkage system. Using the above-mentioned spline functions for $T_k(\theta)$, we calculated the torque applied to the striking body through the linkage system using the following relationship (Fig. 1D):

$$\tau_{applied} = -\frac{\tau_{spring}}{T_k} . \qquad (6)$$

This torque was considered to act at joint **b** on the striking body, which we modeled as a pin joint with a fixed position in the global frame of reference. This assumes that translation of the proximal base of the striking body (at **b**) has a negligible influence on strike dynamics. We evaluated this assumption with the preliminary results of a more complicated model that allowed translation. Considering the particular geometry of *G. smithii* four-bar linkage, we found that the kinetic energy created by translation was more than two orders of magnitude below the kinetic energy generated by rotation. By neglecting this small component of motion, the mathematics of our model were greatly simplified.

We modeled the torque created by drag on the striking body with a blade-element approach that integrates the force generated by elements along the length of the striking body (Patek et al., 2004). This torque was calculated with the following equation (Hoerner, 1965):

$$\tau_{drag} = -0.5\rho_{water}DH^5\left(\frac{d\gamma}{dt}\right)^2 , \qquad (7)$$

where ρ_{water} is water density ($1024\,kg\,m^{-3}$), $d\gamma/dt$ is the speed of output angle rotation, H is the total length of the striking body and D is the drag torque index. We define the drag torque index as a dimensionless parameter that indicates the capacity for the shape of the striking body to generate torque from drag. We calculated this parameter by approximating the shape of the striking body as an elliptical cylinder, which we varied by modifying its dimensions along its length. The drag torque index was calculated with the following integral:

$$D = \frac{1}{l_{SB}^5} \int_0^{l_{SB}} C_d T r^3 \, dh_{dac} , \qquad (8)$$

where each element has a position along the length of the dactyl, h_{dac} (up to the total length of the striking body, l_{SB}), a width, T (perpendicular to flow), a distance from **b**, r, and a drag coefficient, C_d. The drag coefficient for an elliptical cylinder at subcritical Reynolds numbers is approximated by the following equation (Hoerner, 1965):

$$C_d = 0.015\left(1 + \frac{C}{T}\right) + 1.1\left(\frac{T}{C}\right) , \qquad (9)$$

where C is the chord width (in the direction of flow) of the elliptical section.

The motion of the striking body is also resisted by its mass. The total mass and the proximity of its center to the axis of rotation determine the degree of the resistance provided by the striking body, as indicated by its moment of inertia, I_{SB}. The striking body also accelerates a mass of water as it moves that provides additional resistance that is proportional to its moment of inertia, I_{water}. As detailed below, I_{SB} was measured from CT scans of the striking body. I_{water} was calculated from the same measurements of T used to calculate drag (Eqns 8 and 9), using the following equation (Sarpkaya, 1986):

$$I_{water} = \frac{1}{4}\pi\rho_{water}\int_0^H r^2 T^2 \, dh . \qquad (10)$$

We formulated an equation for the dynamics of the striking body as the basis for our simulations. This governing equation was

formulated as the sum of torques acting at **b**, set equal to the product of the moment of inertia and the rotational acceleration:

$$\frac{d^2\gamma}{dt^2} = \frac{\tau_{\text{applied}} + \tau_{\text{drag}}}{I_{\text{water}} + I_{\text{SB}}} \ . \tag{11}$$

This is a second-order, ordinary differential equation, where torque generated by drag (τ_{drag}) depends on the square of $d\gamma/dt$ (Eqn 7) and τ_{applied} depends on θ, which varies with γ (Eqns 5 and 6).

We simulated individual strikes by finding solutions to the governing equation numerically. This was achieved with an explicit fourth-order Runge–Kutta method [the 'ode45' function in MATLAB, based on Dormand and Prince (Dorman and Prince, 1980)], with a zero initial velocity and an initial position (γ_0) that was calculated [using spline functions for $\gamma(\theta)$, described above] from the initial position of the meral-V (θ_0). For each simulation we calculated the angular momentum, L, as follows:

$$L = \left(I_{\text{water}} + I_{\text{SB}}\right)\frac{d\gamma}{dt} \ . \tag{12}$$

We used this calculation to test the accuracy of our simulations against strike impulse measurements (described below). This was achieved by estimating the linear momentum, P, of the striking body at the time of impact as $P=L/h_{\text{out}}$, where h_{out} is the distance between **b** and of the center of mass of the striking body. This distance was calculated with the following equation (McHenry, 2011):

$$h_{\text{out}} = \sqrt{\frac{I_{\text{water}} + I_{\text{SB}}}{m}} \ . \tag{13}$$

Strike energetics

For each of our simulations, we calculated strike energetics to examine how the morphology of the raptorial appendage affects the efficiency of a strike. The elastic energy stored within the meral spring was calculated with the following equation:

$$E_{\text{elastic}} = \frac{1}{2}k_{\text{torsion}}(\theta - \theta_{\text{rest}})^2 \ . \tag{14}$$

We calculated the kinetic energy of the striking body with the following equation:

$$E_{\text{kine}} = \frac{I_{\text{water}} + I_{\text{SB}}}{2}\left(\frac{d\gamma}{dt}\right)^2 \ . \tag{15}$$

The power output of the striking body was calculated as the first time derivative of kinetic energy. The energy lost from the appendage due to drag was calculated with the following equation:

$$E_{\text{drag}} = \rho_{\text{water}}C_D A \int_{\gamma_0}^{\gamma_t}\left(\frac{d\gamma}{dt}\right)^2 d\gamma \ , \tag{16}$$

where γ_0 and γ_t are the output angles at the start and at time t, respectively.

We considered strike energetics for versions of our model that both included and excluded drag. In the absence of drag, energy conservation was assumed and the ultimate rotation speed generated by the striking body was predicted by setting the elastic energy at the start of the strike equal to the kinetic energy at the end of the strike (i.e. when the meral spring has reached its resting position). This equality permits the following prediction of the maximum rotation speed for a simulation without drag (McHenry, 2011):

$$\left(\frac{d\gamma}{dt}\right)_{\text{max}} = \left(\theta_0 - \theta_{\text{rest}}\right)\sqrt{\frac{k_{\text{torsion}}}{I_{\text{SB}} + I_{\text{water}}}} \ , \tag{17}$$

where θ_0 is the initial position of the meral spring. From this equation, the maximum angular momentum generated by the striking body, L_{max}, may be calculated as the product of I_{SB} and Eqn 17:

$$L_{\text{max}} = \left(\theta_0 - \theta_{\text{rest}}\right)\sqrt{k_{\text{torsion}}(I_{\text{SB}} + I_{\text{water}})} \ . \tag{18}$$

Energy conservation was not assumed in simulations that considered the drag generated on the striking body. In this version of the model, drag acts to reduce the efficiency of a strike. We calculated this effect of drag with the transmission efficiency, η, defined by the following equation:

$$\eta = \frac{E_{\text{kine,max}}}{E_{\text{elastic,max}}} \ . \tag{19}$$

Measurements

We conducted a series of measurements to provide parameter values for our model and to test its accuracy. For these measurements, individuals of *Gonodactylus smithii* Pocock 1893 were collected on Lizard Island, Queensland, Australia (Great Barrier Reef Marine Parks Permit #G07/23055.1) and transported to the University of California, Berkeley, for experimentation. The animals were maintained in individual plastic cups (2l) with artificial seawater (salinity: 32–36 ppt; 22°C) and were fed fresh grass shrimp twice per week until strike impulse experiments were performed (described below). Materials tests were then conducted to establish the stiffness of the meral spring (described below). Body length and body mass were measured for each individual. A total of 10 animals (five males and five females), ranging from 58 to 64 mm in length, were used.

Four-bar linkage geometry

The geometry of the linkage system was determined from coordinates that were visually selected from high-resolution photographs of the raptorial appendage (12 megapixel DSLR camera, Nikon D300, AF Micro-NIKKOR 60 mm f/2.8D or 105 mm f/2.8D macro lenses, Nikon Inc., Melville, NY, USA; and EM-140 DG macro-flash, Sigma Corp., Ronkonkoma, NY, USA) (Fig. 2A). The lateral sides of the left and right appendages were each photographed three times and we used the mean values of coordinates recorded from all of these measurements. The four coordinates for the four-bar linkage (**a–d** in Fig. 1B) were recorded with the software TpsDig2 (Rohlf, 2005) for the morphology in its loaded configuration (i.e. the coordinates of the meral-V were rotated proximally after digitizing to represent the contracted configuration of the four-bar linkage).

Stiffness measurements

We measured the stiffness of the meral spring that drives the motion of the raptorial appendage. Measurements were performed as in previous studies (Zack et al., 2009; Claverie et al., 2011) by pulling the carpus and the meral-V towards the merus – the same movement as performed by living mantis shrimp prior to a strike (Patek et al., 2007). Force-displacement measurements on the spring were acquired using a materials testing machine (Blue Hill v. 2.12 Instron model 5544, Instron Corp., Canton, MA, USA; load cell model 2530-416, 0.5 kN maximum, 0.125 N resolution or 0.25% of load). As previously reported (Zack et al., 2009), the force created by the meral spring may be approximated as a linear function of
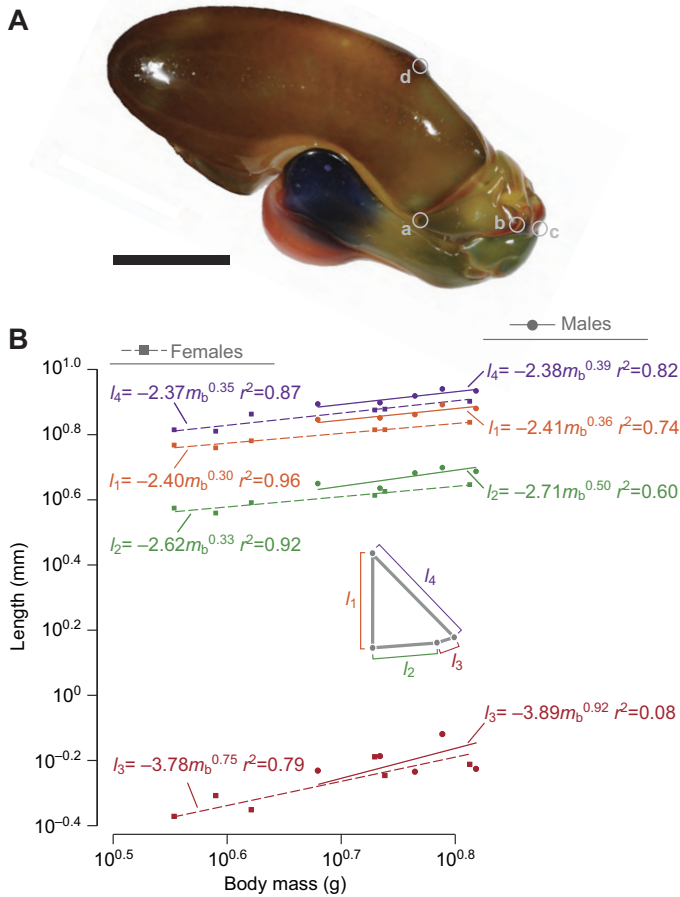
A

B

Fig. 2. The measurement and scaling of linkage lengths in the raptorial appendage. (A) Coordinates measured from digital photographs of the raptorial appendage provided morphometrics for the four-bar linkage system and striking body. Scale bar, 5 mm. (B) The lengths of each of the links in the system (Table 1) plotted with log-transformed axes demonstrates their scaling with respect to body mass. The schematic drawing of the four-bar linkage provides the color-coding for each link length (l_1 in orange, l_2 in green, l_3 in red, and l_4 in purple) for both females (squares and dashed lines) and males (circles and solid lines). The linear fits and their corresponding equations were determined by reduced major axis regression (see Table 2 for descriptive statistics).

displacement with a slope equal to the linear spring stiffness, k_{linear}. We transformed these measurements of linear stiffness into torsion spring stiffness ($k_{torsion}$) for our model, using the following equation:

$$k_{torsion} = k_{linear} h_{load}^2 \cos(\vartheta) , \qquad (20)$$

where h_{load} is the distance between the base of the meral-V (**a**; Fig. 1B) and the point of force application on the carpus and υ is the angle between the direction of the load and the meral-V (link 2; Fig. 1C). This relationship assumed that the deflections are small relative to h_{load}. We measured υ and h_{load} before loading began from video stills of the materials testing setup using ImageJ (National Institutes of Health, Bethesda, MD, USA).

Striking body morphology

We used density and shape information from CT scans to measure the moment of inertia (I_{SB}) of the striking body. CT scans of the carpus, dactyl and propodus were acquired at Harvard University Center for Nanoscale Systems (Model HMXST225, X-Tek, Nikon Metrology NV, Leuven, Belgium). Images were analyzed and

produced using 3-D reconstruction software (VGStudio Max v. 2.0.5, Volume Graphics GmbH, Heidelberg, Germany). The pixel intensity of voxels within a CT scan indicates the radiodensity of a sample, which is proportional to the mass density of biological tissues, ρ_{tissue} (kg m^{-3}) [i.e. $\rho_{tissue} = C_{pix} p$, where p is pixel intensity (dimensionless) and C_{pix} is a constant (kg m^{-3})] (Seeram, 2000). Therefore, I_{SB} may be calculated from a CT scan using the following equation:

$$I_{SB} = vC_{pix} \sum_{i=1}^{n} r_{vox,i}^2 p_i , \qquad (21)$$

where v is the volume of voxel i, n is the total number of voxels, and r_{vox} is the distance between the voxel and the axis of rotation (at **b**; Fig. 1C). We identified the medial and lateral joint articulations between the carpus and merus as the point of rotation for the dactyl plus the propodus. CT scans can provide a measure of the total mass of a specimen with the following relationship:

$$m_{SB} = vC_{pix} \sum_{i=1}^{n} p_i . \qquad (22)$$

We used Eqns 21 and 22 to formulate a non-dimensional moment of inertia, I_{SB}^*, for the striking body ($I_{SB} = I_{SB}^* m_{SB} H^2$, where m_{SB} is the mass of the striking body) that varies with the shape, but not the size of the structure. We defined this quantity as follows:

$$I_{SB}^* = \frac{\sum_{i=1}^{n} r_i^2 p_i}{H^2 \sum_{i=1}^{n} p_i} , \qquad (23)$$

where H is the total length of the striking body. This measure of the moment of inertia has the advantage of not requiring the calibration of the CT scans for tissue density (i.e. measuring C_{pix}). Furthermore, I_{SB}^* allows for the moment of inertia to be defined in our modeling for a striking body of any size if the mass and dactyl length are known. We measured I_{SB}^* from three scans of striking bodies of different size (m_{SB}=31.6, 211.0 and 402.2 mg and H=0.57, 1.10 and 1.27 cm, respectively).

Measurements of the shape of the striking body were used to calculate the drag torque index (Eqn 8). This was achieved by thresholding images of the striking body from head-on and side views to produce a binary image with the striking body appearing black on a white field. This procedure and masking of the proximal section of the appendage was completed in Photoshop (CS5, Adobe, San Jose, CA, USA). We then analyzed the contours of these images to calculate the chord width (C) and width (T) of the striking body along its length.

Scaling analysis

Morphological parameters of the raptorial appendage have the potential to vary with the size and sex of a mantis shrimp (Claverie et al., 2011). In order to consider the scale-dependency of the dynamics of the raptorial appendage, we measured the scaling of parameters in our model (carapace length, total length, l_1, l_2, l_3, l_4, H, θ_0, θ_{rest}, $k_{torsion}$, D and $T_{k,min}$) with respect to body mass (m_b) for individuals of each sex. Each parameter was considered to have the potential for exponential scaling, as given in the following relationship:

$$y = Am_b^B , \qquad (24)$$

where y is a morphological parameter, B is the scaling factor and A is a scaling constant. We performed a reduced-major axis

Table 1. Measured parameters used in the mathematical model

Individual	m_b (g)	m_{SB} (g)	CL (mm)	TL (mm)	l_1 (mm)	l_2 (mm)	l_3 (mm)	l_4 (mm)	H (mm)	θ_0 (deg)	θ_{rest} (deg)	$T_{k,min}$	$k_{torsion}$ (N m deg^{-1})	D
Female														
1	4.18	0.204	14.5	58.6	6.04	3.90	0.45	7.30	10.48	85.0	99.2	6.9	0.012	0.074
2	5.47	0.230	15.5	63.4	6.54	4.23	0.57	7.56	10.90	80.0	92.3	6.1	0.010	0.076
3	5.36	0.202	15.6	65.4	6.53	4.11	0.65	7.51	12.37	80.0	92.5	6.9	0.008	0.073
4	6.50	0.249	16.2	67.7	6.89	4.44	0.61	7.99	10.45	80.4	92.9	5.2	0.030	0.062
5	3.89	0.145	13.9	56.1	5.75	3.63	0.49	6.47	11.18	78.4	91.6	5.9	0.013	0.075
Mean±1 s.d.	5.08± 1.06	0.206± 0.039	15.2±0.9	62.3±4.8	6.35± 0.45	4.06± 0.31	0.55± 0.08	7.36± 0.56	11.08± 0.78	80.7± 2.5	93.7± 3.1	6.2± 0.7	0.015± 0.009	0.072± 0.006
Male														
6	6.58	0.342	16.9	66.6	7.60	4.87	0.59	8.60	11.36	78.8	91.8	5.6	0.015	0.066
7	5.42	0.262	15.9	63.7	7.10	4.32	0.65	7.91	11.73	77.6	93.4	6.9	0.015	0.068
8	5.82	0.290	16.4	63.8	7.28	4.81	0.58	8.29	12.10	78.4	90.6	5.5	0.010	0.074
9	6.15	0.320	17.3	66.0	7.80	5.00	0.76	8.72	11.44	77.4	91.5	6.5	0.020	0.075
10	4.78	0.268	15.3	59.0	7.02	4.47	0.59	7.84	9.41	76.6	89.5	6.2	0.014	0.074
Mean±1 s.d.	5.75±. 0.69	0.296± 0.034	16.4± 0.8	63.8± 3.0	7.36± 0.33	4.69± 0.29	0.64± 0.08	8.27± 0.39	11.21± 1.05	77.8± 0.8	91.4± 1.5	6.1± 0.6	0.015± 0.003	0.072± 0.004

CL, carapace length; D, drag torque index; H, dactyl length; $k_{torsion}$, torsion spring stiffness; l_1–l_4, length of links 1 to 4; m_b, body mass; m_{SB}, mass of striking body; $T_{k,min}$, minimum kinematic transmission; TL, total length; θ_0, starting position of meral-V; θ_{rest}, resting position of meral-V.

regression on log-transformed values of body mass and each parameter in order to find values for *A* and *B*. The degree of certainty in these values was determined by calculating values of lower and upper 95% confidence intervals (CIs). Scaling was considered isometric if the 95% CIs included the scaling factor predicted by isometry, B_{iso} (Rayner, 1985; Sokal and Rohlf, 1995). For example, linear dimensions were predicted to scale to the 1/3 power of body mass (i.e. B_{iso}=1/3), but angles and dimensionless parameters were predicted to be invariant with mass (i.e. B_{iso}=0).

Strike impulse measurements

Impact force was measured from a three-axis force sensor (stainless steel, 16.5 mm diameter load surface, 170 N μm^{-1} stiffness for the *x*- and *y*-axes and 740 N μm^{-1} for the *z*-axis, force range between 2 N and 2 kN, Model 9017B, linked to a charge amplifier model 5073B; Kistler Instruments, Winterthur, Switzerland) that was struck by each individual at least 10 times. Data were collected at 500 kHz using a data acquisition board (NI USB-6251, National Instruments, Austin, TX, USA). We recorded the natural frequency

of the submerged transducer to be 23.4 kHz, which is more than 100 times the frequency calculated from the period of impact (mean±s.d.=0.15±0.13 kHz). We calculated the impulse of a strike by numerically integrating the peak force generated by the initial impact. The mean values and 95% CIs of measurements of strike impulse were compared with model predictions of linear momentum and thus used to validate the model.

RESULTS
Measurements

We examined the scaling of the four-bar linkage system for both males and females of *G. smithii*. With only one exception, morphological parameters for both sexes (Table 1) were found to scale isometrically with respect to body mass (Table 2). The only exception was $T_{k,min}$, which approximately scaled with body length (*B*≈1/3; Table 2), rather than the isometric prediction (B_{iso}=0). In addition, we found that all linkage lengths in *G. smithii* were sexually dimorphic, with males possessing slightly larger linkage lengths than females of comparable size (Fig. 2).

Table 2. Reduced major axis regression of model parameters with respect to body mass; $y=Am_b{}^B$

Variable; y	Units	B_{iso}	Females A Mean	Females A L_1	Females A L_2	Females B Mean	Females B L_1	Females B L_2	Males A Mean	Males A L_1	Males A L_2	Males B Mean	Males B L_1	Males B L_2
CL	mm	1/3	0.99	0.98	1.00	0.27	0.21	0.33	0.94	0.90	0.92	0.36	0.12	0.67
TL	mm	1/3	1.52	1.51	1.53	0.38	0.29	0.49	1.51	1.50	1.52	0.38	0.20	0.58
l_1	mm	1/3	−2.40	−2.41	−2.39	0.30	0.18	0.41	−2.41	−2.42	−2.39	0.36	0.02	0.71
l_2	mm	1/3	−2.62	−2.63	−2.61	0.33	0.19	0.46	−2.71	−2.74	−2.68	0.50	−0.08	1.08
l_3	mm	1/3	−3.78	−3.83	−3.74	0.75	0.28	1.22	−3.89	−3.97	−3.82	0.92	−0.70	2.54
l_4	mm	1/3	−2.37	−2.39	−2.36	0.35	0.15	0.54	−2.38	−2.39	−2.36	0.39	0.09	0.69
H	mm	1/3	−2.18	−2.20	−2.17	0.29	0.11	0.48	−2.15	−2.17	−2.14	0.30	0.05	0.55
θ_0	deg	0	1.82	1.80	1.84	0.13	−0.05	0.31	1.82	1.81	1.83	0.09	0.00	0.18
θ_{rest}	deg	0	2.06	2.04	2.08	0.13	−0.05	0.32	1.86	1.85	1.87	0.13	−0.09	0.35
$k_{torsion}$	N m deg^{-1}	0	−1.43	−1.66	−1.20	1.93	−0.57	4.43	−1.49	−1.65	−1.34	1.86	−1.41	5.13
D		0	−0.91	−0.94	−0.88	0.32	−0.02	0.65	−0.78	−0.82	−0.74	0.49	−0.34	1.31
$T_{k,min}$		0	1.17	1.12	1.22	**0.56**	0.02	1.09	0.92	0.90	0.93	**0.39**	0.12	0.67

A, scaling factor; B, scaling exponent; B_{iso}, isometric prediction; CL, carapace length; D, drag torque index; H, dactyl length; l_1–l_4, length of links 1 to 4; L_1, lower 95% confidence interval; L_2, upper 95% confidence interval; m_b, body mass; $k_{torsion}$, torsion spring stiffness; $T_{k,min}$, minimum kinematic transmission; TL, total length; θ_0, starting position of meral-V; θ_{rest}, resting position of meral-V.
Boldface denotes scaling relationships that are outside the 95% confidence intervals predicted by isometry.
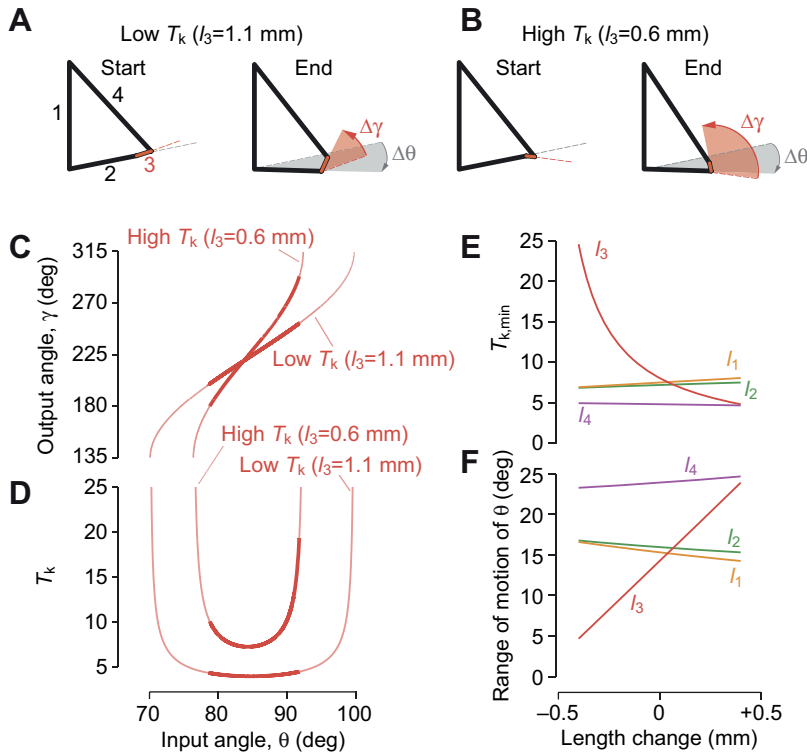
Fig. 3. Gearing by the four-bar linkage system. T_k was examined using parameter values for a single mantis shrimp (individual 3, Table 1) and then by individually varying the length of the links. (A–D) Low- and high-T_k models were created by respectively increasing and decreasing the length of link 3 (l_3). (A,B) The change in shape by the four-bar linkage system from the start to the end of a strike illustrates the displacements of the input ($\Delta\theta$) and output ($\Delta\gamma$) angles for systems with a relatively low T_k (A) and high T_k (B). (C) Values of γ were determined computationally for the full range of θ values theoretically possible (thin curves) for the high- and low-T_k systems. The thick curves illustrate the range of observed values: from the starting (loaded) to resting positions. (D) T_k was calculated from the curves in C for the same range of θ values. (E,F) The effect of individually varying the length of each link on the maximum range of motion for the minimum value of T_k (E) and the theoretically possible range of motion in θ (F). Additional symbol definitions are provided in the List of symbols and are described in the Materials and methods.

We examined how T_k changes over the range of motion for linkage systems of different geometry. The geometry was altered in these comparisons by varying the length of individual links about the measured values (Table 1). The linkage system was modeled as a massless component of the system, such that these changes in linkage lengths influenced only T_k and not our calculations of the moment of inertia or hydrodynamic forces. Low- and high-T_k systems were created by respectively increasing and decreasing l_3 beyond measured values by 0.25 mm (Fig. 3A,B). For the same input displacement ($\Delta\theta$), the high-T_k system exhibited a much larger output displacement ($\Delta\gamma$) than the low-T_k system (Fig. 3A,B). The relationship between input and output displacements is non-linear, as revealed by calculating the output angle predicted over the range of possible input values (Fig. 3C). The T_k calculated from this relationship (Fig. 3D) exhibited a U-shaped curve, where T_k may theoretically be increased by either increasing or decreasing the input angle beyond the value for minimum T_k. For a high-T_k system, T_k exhibited a pronounced increase within the range of motion measured for *G. smithii*. In contrast, a low-T_k system did not achieve substantial change in T_k over the same range (Fig. 3D). We found that a reduction in l_3 caused change in $T_{k,min}$ with a strong non-linear dependency not exhibited in any of the other linkage lengths (±0.5 mm; Fig. 3E). Because of the strong sensitivity of T_k to differences in link 3, we manipulated l_3 in our subsequent simulations to evaluate the effects of T_k. The implications of these changes in geometry to the range of motion were also determined (Fig. 3F).

The capacity of a raptorial appendage to generate drag was indicated by the drag torque index, D. According to our blade-element model of drag, the striking body encounters resistive torque in proportion to D (Eqn 7). To calculate this index for an appendage, we used photographs of the striking body (Fig. 4A,B) to measure the chord width and thickness along the dactyl length from silhouettes of the side (Fig. 4C) and head-on (Fig. 4D) views. These measurements (Fig. 4E) provided the basis for calculations of the drag coefficient, C_d (Eqn 9), at each position along the length of the striking body (Fig. 4F). The drag torque index (Eqn 8) was calculated as the integral of the product $C_d Tr^3$ along the length of the striking body (Fig. 4G). This was achieved for all individuals modeled (Table 1) to yield a mean drag torque index of 0.072 (95% CI=0.069, 0.075, N=10), with no significant differences due to body size or sex (Table 2).

We used CT scans to measure the non-dimensional moment of inertia for the striking body (Fig. 5A,B). Our three specimens spanned more than an order of magnitude in mass, yet yielded I^* with similar values (0.26, 0.31 and 0.28; Fig. 5C) that produced a mean value with relatively small 95% confidence intervals (I^*=0.28, 95% CI=0.22, 0.35). This value is not significantly different than a uniform slender rod of uniform density (I^*=1/3) (Meriam and Kraige, 1997). Therefore, the mass distribution of the striking body is similar to a homogenous structure, despite the substantial variation in the distribution of high-density calcified regions that we observed within the striking body (Fig. 5B).

Materials testing experiments determined the stiffness of the meral spring. The mean stiffness for males ($k_{torsion}$=0.014 N m deg^{-1}, 95% CI=0.006 and 0.020 N m deg^{-1}, N=5) was not significantly different from that of females ($k_{torsion}$=0.015 N m deg^{-1}, 95% CI=0.010 and 0.019 N m deg^{-1}, N=5; Table 1). Within each sex we found relatively minor variation among individuals that showed no significant effect of body size (Table 2).

Force measurements were used to determine the strike impulse generated by a raptorial appendage (Fig. 6A). The strike impulse was calculated as the integrated area within the initial force peak created upon impact (Fig. 6B); the mean impulse was 3.1 g m s^{-1} (95% CI=1.3, 4.9 g m s^{-1}, N=10). These measurements provided a basis for testing the accuracy of our mathematical model. From these results, we calculated the momentum of the striking body (Eqn 12) generated by changes in the output angle (Fig. 6D) and interpreted the maximum of these values as the predicted strike impulse. The mean value of this prediction (2.2 g m s^{-1}, N=10) and its 95%
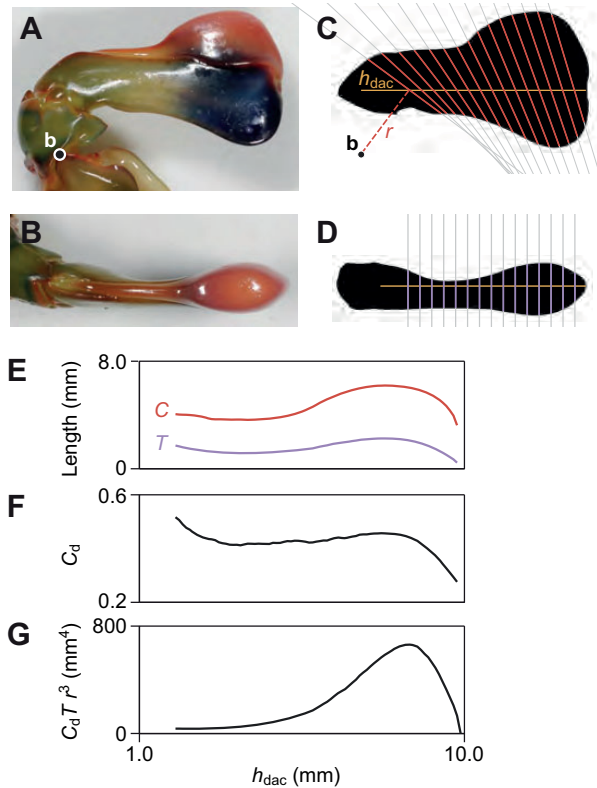
Fig. 4. Measurements of the drag torque index of the striking body of a representative individual. Photographs of the striking body, as viewed from the side (A) and head-on (B) were used to measure the dimensions of the appendage with respect to position along the dactyl, h_{dac}. The highlighted circle denotes **b**, the point of rotation for the striking point (see Fig. 1B). (C,D) Measurements of chord width (C), thickness (T) and distance from **b** (r) were measured at regular intervals along the long axis of the dactyl. (E) These measurements of chord width and thickness provided the basis for calculating (F) the drag coefficient (Eqn 9) and (G) the product $C_d Tr^3$ as a function of h_{dac}. This product was numerically integrated to find the drag torque product for this individual (D=2060 mm^5, Eqn 8). Additional symbol definitions are provided in the List of symbols and are described in the Materials and methods.
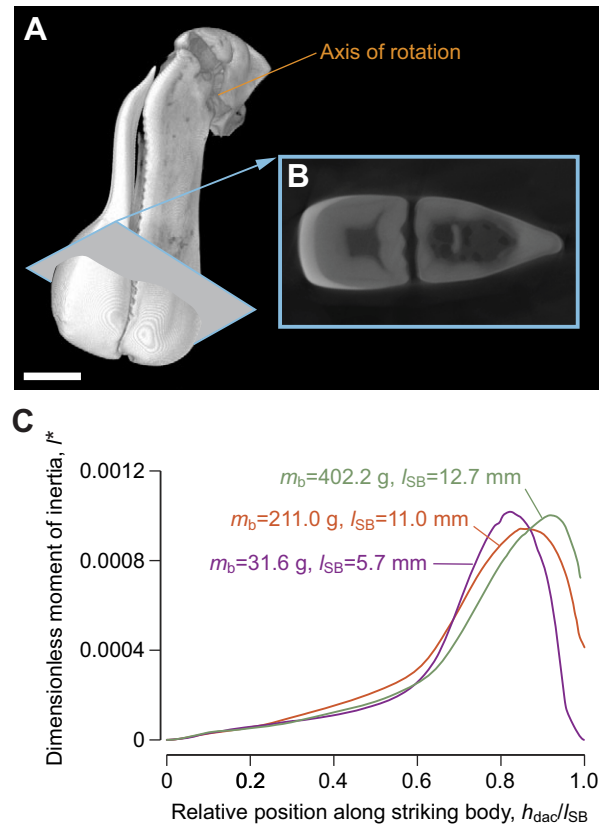

Fig. 5. Micro-computed tomography (CT) scans of the striking body were used to calculate the dimensionless moment of inertia. (A) A rendering of one of the CT scans (scale bar, 2 mm), with the axis of rotation highlighted (orange line, corresponding to **b** in Fig. 1B). A representative transverse section (in gray with blue border) is shown as an inset (B) that reveals the tissue density (proportional to pixel intensity) in the interior of the structure. (C) The dimensionless moment of inertia (I^*) was calculated for each of these images, along the length of the dactyl (where h_{dac} is the position along the dactyl and l_{SB} is the total length). The dimensionless moment of inertia for the entire striking body (Eqn 23) was calculated as the sum of these values. This procedure was conducted on three samples (purple is the smallest and green the largest) that spanned more than a factor of 2 in length and 10 in mass from different individuals.

confidence intervals (1.7, 2.7 g m s^{-1}) were within the 95% confidence intervals of the measurements and therefore not significantly different (Fig. 6E). By this criterion, the model provides an accurate approximation of the dynamics of the strike by a raptorial appendage.

Mathematical model

Our simulations provided the opportunity to examine the energetics over the time course of a strike. The elastic energy stored within the meral spring at the start of a strike was converted into kinetic energy and lost to drag as the striking body moved through the water (Fig. 7A). In contrast, all energy stored within the meral spring was converted to kinetic energy in simulations that did not include drag (Fig. 7B). Drag generates inefficiency in the conversion from elastic to kinetic energy by two mechanisms. First, the creation of E_{drag} (energy due to drag) necessitated a direct loss of energy from the appendage to the surrounding water. Second, as more energy was lost to drag, the timing of peak kinetic energy occurred earlier in the strike. As a consequence, the meral spring did not reach its resting length at the moment of maximum angular velocity, and therefore

fails to release all of its stored energy at the time of peak kinetic energy (Fig. 7A).

The effects of elastic energy storage on strike performance were investigated by running a series of simulations with variable amounts of elastic energy within the meral spring prior to the strike. We conducted a set of 10 simulations that each began at the parameter values for a particular individual (Table 1). Each simulation in a set differed by only the spring stiffness, which we increased at even intervals up to 0.013 N m deg^{-1} above the measured value. For example, we ran a series for individual 4 using its measured parameter values ($k_{torsion}$=0.030 N m deg^{-1}, purple curve in Fig. 8) and then repeated simulations with incrementally increased spring stiffness (up to $k_{torsion}$=0.043 N m deg^{-1}). In simulations without drag, the calculated speed and momentum (Fig. 8A,B) were predictable from our analytical model of strike energetics. This model shows that both rotation speed and angular momentum varied with the square root of spring stiffness (Eqns 17 and 18). Although drag decreased the speed and momentum of simulated strikes, spring stiffness had a similar effect on these variables (Fig. 8Aii,Bii) as in the simulations without drag (Fig. 8Ai,Bi). In simulations both with
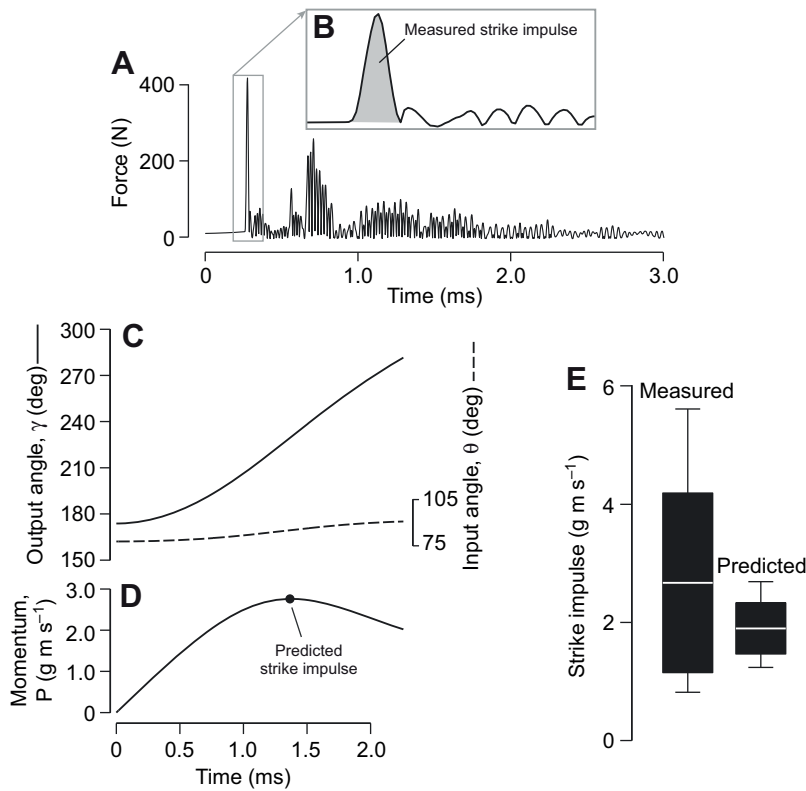
Fig. 6. The measured strike impulse was compared with the prediction formulated from our mathematical model. (A) A representative rectified force recording (from individual 7, Table 1) illustrates a strike impulse calculation. (B) Strike impulse was calculated as the time integral of the maximum force peak near the start of the impact ($0.95\,\mathrm{g\,m\,s^{-1}}$). (C) A representative strike simulated by our mathematical model, where the output (γ) and input (θ) angles were determined by solving the governing equation (Eqn 11), which models the torques that act on the striking body. (D) The linear momentum (P) for this simulation was calculated (Eqn 12) to formulate a prediction of the strike impulse. The predicted impulse was calculated as the maximum value for linear momentum (filled circle). (E) The model predicts values for strike impulse that are similar to what was measured. The bars denote the 95% confidence intervals about the mean (white line) with the error flags denoting the range of values.

and without drag, the time to reach maximum rotation speed decreased monotonically with stiffness (Fig. 8C) because greater spring stiffness created a larger torque to rotate the striking body (Eqns 5 and 6).

Similar to our investigation into the effects of spring stiffness, we ran a series of simulations that varied the mass of the striking body (Fig. 9). This manipulation influenced the governing equation (Eqn 11) by changing the moment of inertia ($I_{SB}=I_{SB}^{*}m_{SB}H^{2}$, where I_{SB}^{*} and H were assumed to be constant). In the absence of drag, rotation speed is inversely proportional to the square root of mass (Eqn 17), and momentum (Eqn 18) is directly proportional to the square root of mass (Fig. 9Ai,Bi). Similar effects of mass were apparent in simulations that included drag (Fig. 9Aii,Bii).

We examined two simulations that demonstrated the effects of a difference in linkage geometry. Both received an equal amount of stored elastic energy, but they differed in T_k because of a difference in the length of link 3 (Fig. 1C). Because of this difference, the high-T_k system swept the striking body with a greater displacement of output angle than a low-T_k system (Fig. 10A). However, the low-T_k system achieved a higher rotation speed (Fig. 10B) and power output (Fig. 10C) over its shorter displacement. This result was a consequence of drag generation. Drag energy (Fig. 10D) was calculated as the integral of the torque created by drag over the output angle displacement (Eqn 17). The low-T_k system spanned a more narrow range of the output angle that generated relatively low drag energy (red area in Fig. 11). Therefore, the low-T_k system generated a higher transmission efficiency (Eqn 20) than the high-T_k system (blue area in Fig. 11).

The effects of T_k on strike performance were further examined with a series of simulations. Similar to the above-described comparison, these simulations began with an equivalent amount of stored elastic energy and differed only in the length of link 3. These simulations revealed that the time to maximum speed increased (Fig. 12A), and the maximum speed of the input angle (Fig. 12B)

and power output (Fig. 12C) decreased monotonically with greater $T_{k,min}$. In simulations without drag, differences in T_k had no effect on the maximum rotation speed (Fig. 12D). However, when drag was included, the maximum rotation speed decreased monotonically
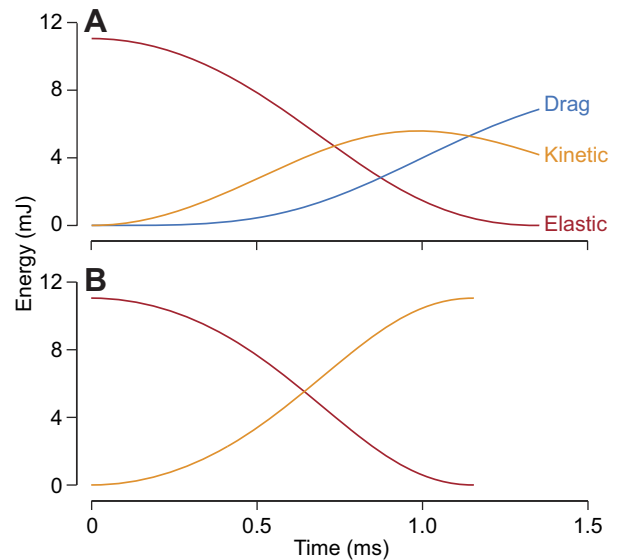

Fig. 7. The energetics of a strike predicted by the mathematical model. These simulations used parameters values for individual 2 (Table 1) and differ only by including (A) or excluding (B) drag. (A) As the striking body swings to execute a strike, the elastic energy (red line) contained within the meral spring is converted into the kinetic energy of the striking body (orange line) and lost through the generation of drag (blue line). (B) A simulation that excludes the drag force demonstrates ideal conversion efficiency ($\eta=1.0$), as all potential energy at the start of the simulation is applied to kinetic energy without loss.
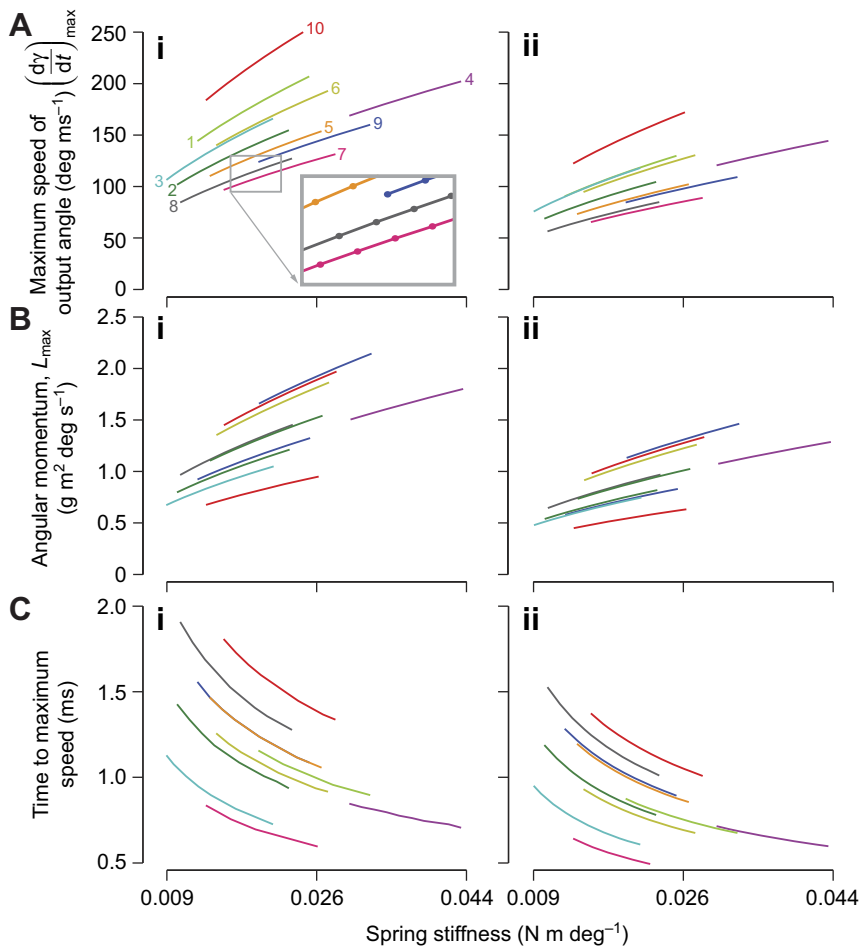
Fig. 8. Effects of spring stiffness on strike performance. Each colored curve represents simulation results for a series of simulations that were based on an individual stomatopod (the numbers in A correspond to individuals listed in Table 1). These results were formulated from 10 simulations that differ only by increasing spring stiffness (up to an additional 0.013 N m deg^{-1}) above the measured value for an individual (Table 1) at even intervals. These simulations were conducted both without (i) and with (ii) drag. For simulations without drag, an analytical model of strike energetics predicted the simulation results for rotation speed (Eqn 17) and momentum (Eqn 18). No analytical solution was found for simulations that included drag. (A) The maximum angular speed predicted during a simulation without drag (i) and with drag (ii). The inset shows how simulation results (points) may be predicted by the analytical model (line; Eqn 17). For each set of simulations, the (B) angular momentum and (C) time required to reach the maximum speed of the striking body are shown. Additional symbol definitions are provided in the List of symbols and are described in the Materials and methods.

with increasing $T_{k,min}$. This trend was attributable to the effect of T_k on transmission efficiency. Linkage systems with greater T_k achieved a greater output angle excursion, causing more energy to be lost to drag (Fig. 11), which caused a reduction in efficiency and, in the end, a slower strike (Fig. 12D).

DISCUSSION

The present study demonstrates that the predatory strike of the mantis shrimp can be modeled from measurements of its morphology and structural properties (Fig. 6). An analysis of this model offers insight into the roles of elastic energy storage, the striking body and the force transmission system in a predatory strike. These results illustrate how the speed of a force transmission system is mediated by transmission efficiency, which is a general principle that may be applied to the biomechanics of a broad diversity of animals.

Elastic energy storage

The rotation speed of a strike is largely determined by the amount of stored elastic energy imparted to the raptorial appendage. The meral spring may theoretically store a greater amount of energy by elevating the stiffness of the spring or increasing its degree of compression prior to the strike (Eqn 14). As a consequence, the maximum speed of output rotation is proportional to the pre-strike compression and the square root of stiffness (Eqn 17) in the absence of drag (Fig. 8Ai), with a similar relationship in the presence of drag (Fig. 8Aii). Therefore, mantis shrimp may have evolved to enhance their strike speed by increasing the elastic storage capacity of the

meral-V and the work output of the extensor muscles that primarily deflect this structure (Claverie et al., 2011).

The architecture of the extensor muscles has likely influenced the evolution of the meral spring. The fibers of these muscles have a pinnate architecture (Burrows, 1969; Burrows and Hoyle, 1972; McNeill et al., 1972), which is a shape that is ubiquitous among crustaceans and is thought to offer an advantage over parallel-fibered muscle because it creates a relatively modest bulging in diameter. This allows a muscle to occupy a relatively large proportion of the cross-sectional area within the rigid exoskeleton (Alexander, 1968). Pinnate muscles generate relatively high force, but must do so over a low strain. Therefore, the extensor muscle likely constrains the range that the meral spring may be deflected in preparation for a strike.

The striking body

A strike is resisted by the inertia and drag torque generated by the striking body. This resistance is largely generated in the distal region, where the striking body's mass and projected area are large (Fig. 5C, Fig. 4D). Despite these effects of shape, the striking body may be approximated by a simple geometry, as in previous models (e.g. Patek et al., 2004). For example, our analysis of CT scans revealed that the dimensionless moment of inertia for the striking body is similar to a cylinder of uniform density ($I^* \approx 1/3$) (Meriam and Kraige, 1997) and this result holds true over more than an order of magnitude in mass (Fig. 5C). Similarly, the torque drag product (Fig. 4) does not vary substantially among individuals (Table 1) and could be approximated by modeling the striking body
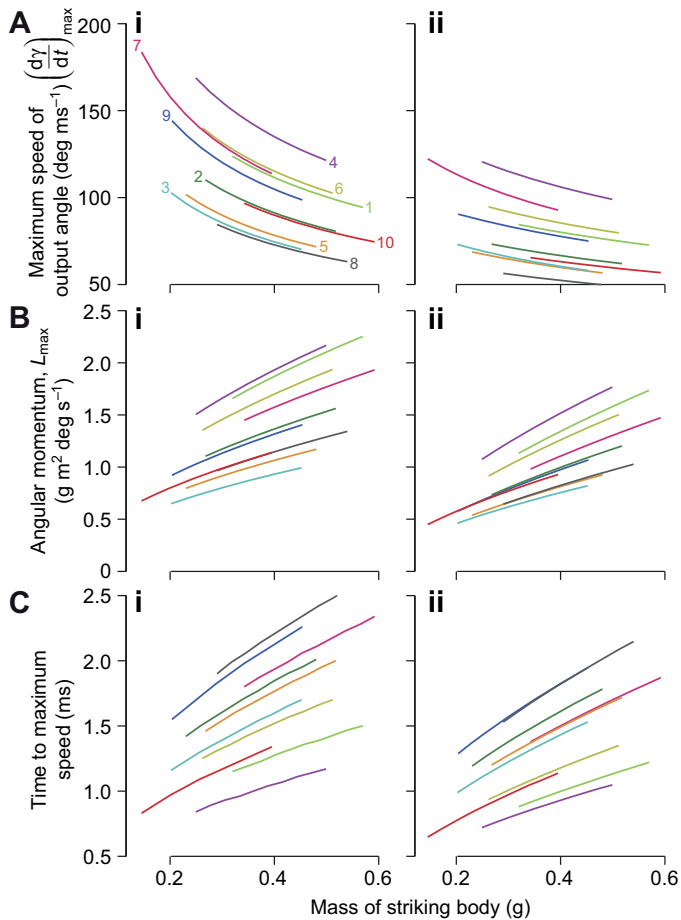
Fig. 9. The effects of differences in the mass of the striking body on strike performance. In these plots, the mass of the striking body was increased (up to 0.25 g) above the measured value for each individual (the numbers in A correspond to individuals listed in Table 1), over 10 simulations at even intervals. Simulations were run both without (i) and with (ii) drag. For simulations without drag, an analytical model of strike energetics predicted the simulation results for speed (Eqn 17) and momentum (Eqn 18). No analytical solution was found for simulations that included drag. For each set of simulations, the (A) maximum angular speed, (B) angular momentum and (C) time required to reach the maximum speed of the striking body are shown. Additional symbol definitions are provided in the List of symbols and are described in the Materials and methods.

as a uniform cylinder. Therefore, differences in the shape of the striking body among individuals of *G. smithii* do not have a large effect on strike dynamics. Given the large morphological diversity among mantis shrimp species (Ahyong, 2001), interspecific differences in the shape of the striking body may have a more substantial influence on the predatory strike than what we have found with a single species.

Our model of drag neglects some fluid forces that could arguably affect strike dynamics. This includes skin friction generated at the distal end of the striking body due to large shear stress in that region. Our blade-element approach also ignores any effect of span-wise flow along the length of the striking body. Although such factors may contribute higher-order effects, the matching of our results with measured kinematics (Fig. 6) suggest that our model offers an accurate first-order approximation of the major forces generated during a strike. Furthermore, additional fluid forces would serve to enhance the loss of energy to drag and thereby produce an even

stronger negative relationship between $T_{k,min}$ and maximum rotation speed (Fig. 12).

Differences in the size of the striking body affect the strike performance of *G. smithii*. The mass and length of the striking body are major factors in the more than twofold range of variation in the maximum rotation speed, angular momentum and time to maximum speed predicted by the model (Fig. 9). Because the strike is modeled as moving with pure rotation, its inertial resistance is determined solely by the sum of the moment of inertia of the striking body (I_{SB}) and the surrounding water (I_{water}, Eqn 10). We varied I_{SB} in a series of simulations that differed only in the mass of the striking body ($I_{SB}=I_{SB}^* m_{SB} H^2$), which yielded analytically predictable results without drag (Eqn 17) and similar results with drag (Fig. 9). These results suggest that large individuals encounter disproportionately high inertial resistance that slows the strike, but the greater mass of the striking body generates more momentum during a strike. Specifically, the angular momentum is nearly proportional to the square root of the moment of inertia (Eqn 18). However, because these higher momentum values are achieved at slower rotation speed (Fig. 9A,B), it would be more difficult for a massive striking body to create the cavitation bubbles that contribute a substantial force when striking prey (Patek and Caldwell, 2005). Furthermore, the torque created by drag scales with length to the power of 5 (Eqn 7), which suggests that a larger striking body may be substantially less efficient than a smaller one.

The linkage system

In the absence of drag, differences in the geometry of the four-bar linkage system have no effect on the speed of rotation for a strike when stored elastic energy is constant. This conclusion is based on the results of a series of simulations run with different $T_{k,min}$ (by varying l_3) and the same amount of stored elastic energy. In simulations that excluded drag, all of the elastic energy at the start of the strike was converted into the kinetic energy of the striking body (Eqn 17), irrespective of differences in $T_{k,min}$ (Fig. 12D). As a consequence, the maximum speed was independent of differences in linkage geometry, where a constant moment of inertia was assumed. Therefore, the maximum rotation speed of an elastic system that conserves energy is independent of geometry whether force transmission is achieved by a linear lever or a four-bar linkage system.

Our simulation that included drag demonstrated that drag causes a loss of energy that substantially affects strike speed. This loss is greater for a high-T_k system, which sweeps the striking body through a longer angular displacement than in a low-T_k system with the same input displacement (Fig. 10A). The angular displacement defines the range over which the drag torque is integrated to determine the energy lost during a strike (i.e. the area under the curve in Fig. 11; Eqn 16). As a high-T_k system transfers relatively more energy to drag, less elastic energy is available for the kinetic energy of the striking body, which slows the strike. This effect is reflected in the transmission efficiency (Eqn 19): increasing $T_{k,min}$ creates a monotonic decrease in the transmission efficiency of a strike, which causes a decrease in maximum power and rotation speed (Fig. 12C,D). Therefore, strike speed is affected by T_k because differences in linkage geometry affect the generation of drag and, consequently, transmission efficiency.

Efficiency in force transmission systems

Our finding that a high-T_k system moves more slowly than a low-T_k system is surprising in the context of some research on skeletal mechanics. As described in the Introduction, the linear speed of a
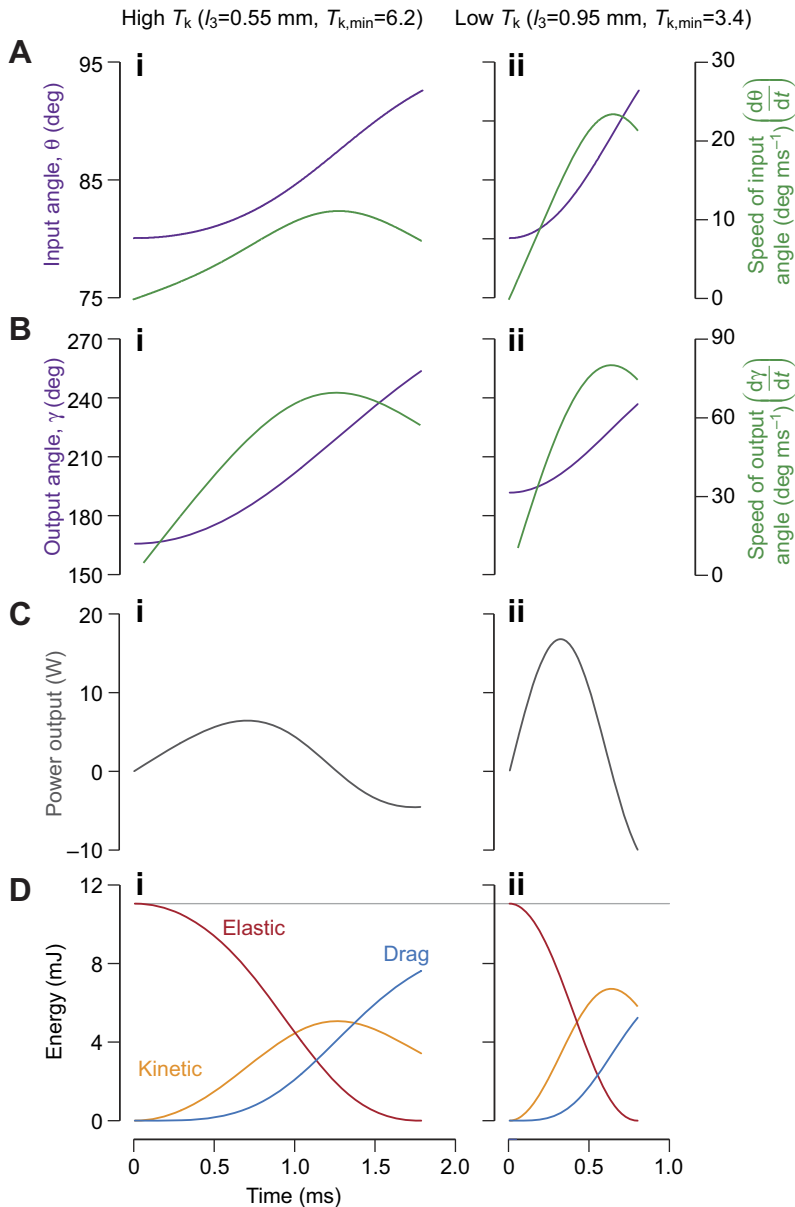
Fig. 10. Simulations that compare the performance of two linkage systems with different T_k. The only parameter that differed between these two simulations was the length of link 3 (Fig. 1C). All other parameter values were set to measured values from a single individual (individual 4, Table 1). The high-T_k simulation (i) was generated by decreasing the length of link 3 ($l_3=0.55$ mm) and the low-T_k simulation (ii) used a longer length for the same link ($l_3=0.95$ mm). (A) Predicted changes in input angle (purple line) and the speed of the input angle (green line) are plotted as a function of time. (B) The corresponding output angle (purple line) and speed of the output angle (green line). (C) The power output of the striking body and the (D) elastic energy (red line), kinetic energy (orange line) and the energy lost to drag (blue line) are plotted. Note that both simulations begin with equivalent stored elastic energy (horizontal gray line). Additional symbol definitions are provided in the List of symbols and are described in the Materials and methods.

simple lever system is related to its displacement advantage, because it is proportional to the ratio of output to input displacement (Gregory, 1912; Smith and Savage, 1956; Hildebrand, 1974). If different levers are actuated with the same input velocity, then their output velocity will be proportional to displacement advantage. Similarly, the velocity of output rotation created by a four-bar linkage system is proportional to T_k, if the input rotation velocity is fixed across differences in geometry (Muller, 1987; Westneat, 1995). Therefore, this gearing-for-speed hypothesis predicts that linkage systems with greater T_k and lever systems with greater displacement advantage should move at faster speeds.

The present model differs from a model that supports the gearing-for-speed hypothesis because we have not assumed that a fixed input velocity drives raptorial appendages of different geometry. Velocity was instead determined by the dynamic torques created by the meral spring and the moment of inertia and drag on the striking body (Fig. 1D). Therefore, our simulations permitted the input velocity and power output to vary with time within a simulation (Fig. 10) and to vary with morphology across simulations (Fig. 12). In all simulations, we provided the force transmission system with an equal

amount of energy, which is particularly appropriate for comparisons of elastically driven systems. Once released, a spring has no inherent constraint on the rate at which it may deliver energy. Therefore, the input velocity for an elastic system was not fixed with respect to time and no *a priori* value for velocity was assumed to model the motion of the system.

Our model further deviates from many previous considerations of lever mechanics by examining the influence of hydrodynamic forces. Drag functions as an energetic sink that reduces the kinetic energy available to the appendage and thereby slows its motion. This effect is indicated by the transmission efficiency, which declines with the higher integrated drag torque created by a linkage system having a relatively high T_k (Fig. 11, Fig. 12D). Therefore, the relationship between the geometry of a force transmission system and its rotation speed is mediated by transmission efficiency.

Transmission efficiency may play a similar role in the feeding apparatus of fishes, which is a classic subject for the study of linkage biomechanics. Like a mantis shrimp, a striking fish predator must accelerate the mass of its skeleton and overcome hydrodynamic forces in order to capture prey. If there is a significant amount of
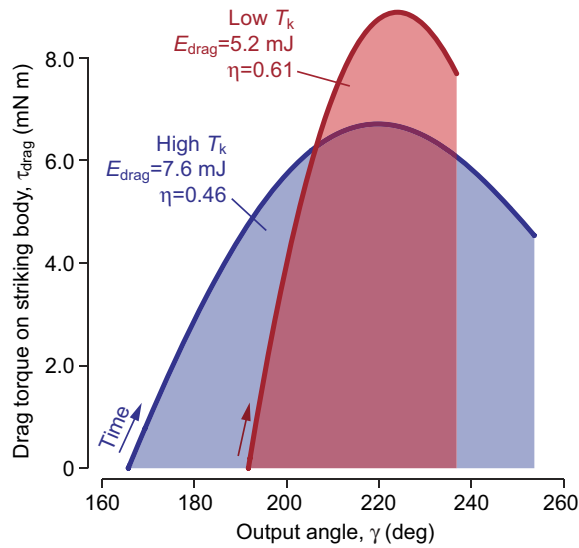
Fig. 11. The generation of drag energy in models that differ in T_k. The torque created by drag is plotted as a function of output angle for the high- and low-T_k simulations displayed in Fig. 10. As the output angle increased in these simulations over time, the drag torque increased. The area under the curve created by these variables is equivalent to the energy lost to drag (Eqn 16). Differences in this loss of energy affect the transmission efficiency of a strike (η; Eqn 19).
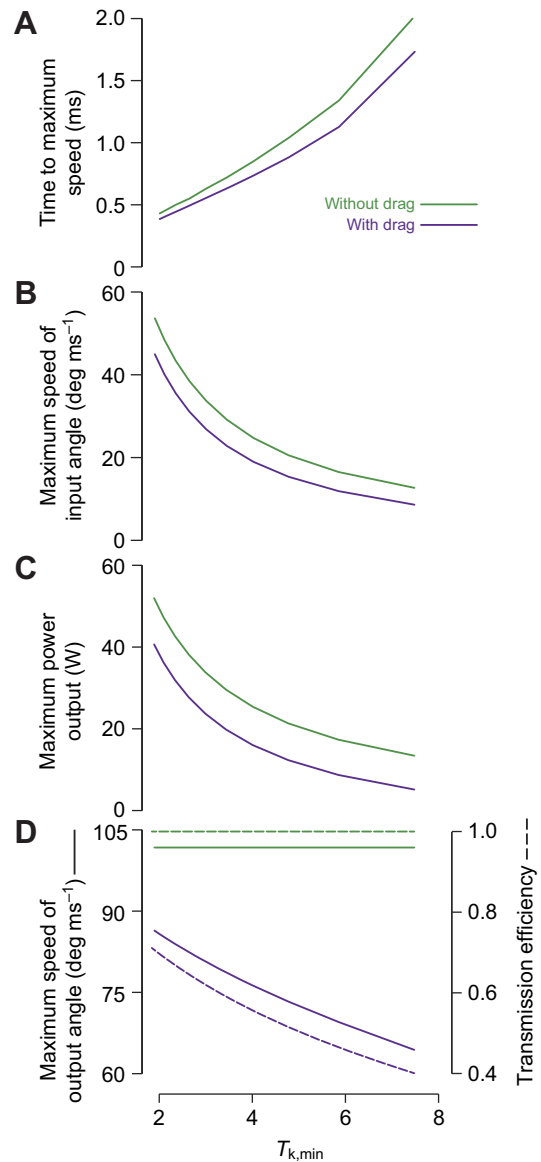

Fig. 12. The effect of T_k on strike performance. Ten simulations were performed with equivalent parameter values (those for individual 3, Table 1), except for an incremental decrease in the length of link 3 (0.54 mm<l_3<0.95 mm) at regular intervals, which served to vary $T_{k,min}$. Therefore, all simulations began with equivalent elastic energy storage (13.2 mJ). These simulations were run both with drag (purple lines) and without drag (green lines). (A) The time to maximum speed is plotted with respect to the minimum T_k generated by each simulation. For the same simulations, the (B) maximum speed of the input angle and (C) the maximum power output of the striking body are plotted. (D) The maximum rotation speed (solid lines) is overlaid with the transmission efficiency (dashed lines).

energy lost to the surrounding water during a strike, then speed may be hindered by a strike exhibiting a high displacement. Therefore, fish species possessing a high-T_k feeding apparatus may be hindered in their ability to move faster, compared with closely related species having lower T_k. Seemingly at odds with this prediction is the observation that fish that feed on evasive prey possess a higher T_k than relatives that feed on slow prey (Westneat, 1995; Wainwright et al., 2004). However, species that prey on evasive prey may not be protruding their jaws any faster than their relatives. Instead, high-T_k species may be taking advantage of the superior displacement of the jaw apparatus that is provided by a high-T_k system. Jaw protrusion has been identified as a major benefit to the performance of suction-feeding predators (Holzman et al., 2008). Although the previous interpretations of evolutionary variation in fish jaw T_k have largely focused on speed as the relevant parameter, it may instead be the benefits conferred by a greater reach that determine the selection for high T_k in fish jaw mechanics.

Transmission efficiency may be an important factor for lever systems in animals that are not aquatic. For example, a toad (*Bufo alvarius*) generates a ballistic mouth opening by storing elastic energy within its depressor mandibulae muscle prior to mouth opening. During the strike, the force generated by this muscle may be modeled as a spring in parallel with a dashpot (Lappin et al., 2006). This dashpot serves to dissipate energy in a manner that is analogous to drag on the raptorial appendage of a mantis shrimp. Unlike drag on an appendage, the toad's energetic loss occurs on the input end of the lever system. Therefore, the transmission efficiency and speed of a toad jaw may be maximized by moving the jaws with a relatively small input displacement. As a consequence, increases in displacement advantage should increase transmission efficiency and result in faster motion.

The significance of transmission efficiency may be different for lever systems that contribute to animal locomotion. Our results suggest that it is beneficial for a predatory strike in a mantis shrimp

to occur over a short distance in order to maximize rotation speed. In contrast, a swimming or flying animal aims to impart momentum to the fluid in order to propel the body forward. It may therefore be advantageous in locomotion to move with a low transmission efficiency by sweeping an appendage over a relatively large excursion.

One of the benefits of examining mechanics and drag in a spring-driven system is the simplicity of such an actuator. A spring generates force in proportion to its length, so the energy that it

imparts to a system consequently does not vary with the rate of length change (Eqn 14). In contrast, muscular force has a non-linear dependency on both length and its rate of shortening (Aidley, 1978). Given that the contractile properties of a muscle govern the energy that may be imparted to a system, the dynamics of skeletal geometry have the potential to yield a different relationship between speed and geometry than that found in the mantis shrimp raptorial appendage in the present study. Despite this possibility, an experimental increase of displacement advantage was recently shown to decrease shortening velocity in the leg of a frog (Richards, 2011). In this system, the force–velocity relationship intrinsic to muscle causes speed to vary with displacement advantage in a manner that is similar to what we have found for the raptorial appendage when loaded with drag.

The central importance of drag in the rotation speed and T_k dynamics of an aquatic mantis shrimp and the organizing principle of transmission efficiency in the evolution of fish jaws strongly suggest that some of the most fundamental assumptions made in biomechanical and functional morphological analyses of speed, force and lever trade-offs may need to be re-examined in the light of the energetics of movement. Perhaps these discoveries will open new doors into the interpretations of evolutionary variation in mechanical systems in biology.

LIST OF SYMBOLS

A	scaling constant
a–d	position vectors for joint positions in four-bar linkage (m)
B	scaling factor
B_{iso}	scaling factor predicted by isometry
C	chord width of an element of the striking body (m)
C_d	drag coefficient (dimensionless)
C_{pix}	density constant (kg m^{-3})
D	drag torque index (dimensionless)
E_{drag}	energy lost to drag (J)
$E_{elastic}$	stored elastic energy (J)
E_{kine}	kinetic energy (J)
H	length of the striking body (m)
$h_{b,d}$	distance between **b** and **d** (m)
h_{dac}	position along the dactyl (m)
h_{load}	distance between the point of loading and **a** (m)
h_{out}	distance between striking body center of mass and **b** (m)
I_{SB}	moment of inertia of striking body (kg m^2)
I^*_{SB}	moment of inertia of striking body (dimensionless)
I_{water}	moment of inertia of the water (m^4)
k_{linear}	linear stiffness of the meral spring (N rad^{-1})
$k_{torsion}$	torsion stiffness of the meral spring (N m deg^{-1})
l_1–l_4	lengths of links in the four-bar linkage (m)
L_{max}	maximum angular momentum of the striking body (kg m^2 deg s^{-1})
l_{SB}	total length of striking body (m)
m_b	body mass (g)
m_{SB}	mass of striking body (g)
p	pixel intensity (dimensionless)
P	linear momentum of the striking body (g m s^{-1})
r	distance between an element of the striking body and **b** (m)
r_{vox}	distance between a voxel and **b** (m)
t	time (s)
T	width of an element of the striking body (m)
T_k	kinematic transmission (dimensionless)
v	volume of voxel
$\hat{\mathbf{x}}$	unit vector (dimensionless)
$\hat{\mathbf{y}}$	unit vector, orthogonal to $\hat{\mathbf{x}}$ (dimensionless)
γ	output angle of the linkage system (deg)
η	transmission efficiency (dimensionless)
θ	input angle of a lever or linkage system (deg)
θ_0	initial position of the input angle (deg)
θ_{rest}	position of the input angle at rest (deg)
ρ_{tissue}	density of tissue (kg m^{-3})
ρ_{water}	density of water (kg m^{-3})
$\tau_{applied}$	torque applied to the striking body (N m)
τ_{drag}	torque generated by drag (N m)
τ_{spring}	torque generated by meral spring (N m)
υ	angle between the direction of the load and the meral-V (deg)
ψ	angle between links 1 and 4 (rad)

REFERENCES

Ahyong, S. T. (2001). *Revision of the Australian Stomatopod Crustacea.* Sydney: Australian Museum.

Aidley, D. J. (1978). *The Physiology of Excitable Cells.* New York: Cambridge University Press.

Alexander, R. M. (1968). *Animal Mechanics.* Seattle, WA: University of Washington Press.

Anker, G. (1974). Morphology and kinetics of the head of the stickleback, *Gasterosteus aculeatus. Trans. Zool. Soc. Lond.* **32**, 311-416.

Barrett, P. M. and Rayfield, E. J. (2006). Ecological and evolutionary implications of dinosaur feeding behaviour. *Trends Ecol. Evol.* **21**, 217-244.

Burrows, M. (1969). Mechanics and neural control of prey capture strike in mantis shrimps *Squilla* and *Helmisquilla. Z. Vergl. Physiol.* **62**, 361-381.

Burrows, M. and Hoyle, G. (1972). Neuromuscular physiology of strike mechanism of mantis shrimp, *Hemisquilla. J. Exp. Zool.* **179**, 379-394.

Claverie, T., Chan, E. and Patek, S. N. (2011). Modularity and scaling in fast movements: power amplification in mantis shrimp. *Evolution* **65**, 443-461.

Daniel, T. L. (1995). Invertebrate swimming: integrating internal and external mechanics. *Symp. Soc. Exp. Biol.* **49**, 61-89.

Dormand, J. R. and Prince, P. J. (1980). A family of embedded Runge-Kutta formulae. *J. Comp. Appl. Math.* **6**, 19-26.

Gregory, W. (1912). Notes on the principles of quadrupedal locomotion and on the mechanism of the limbs in hoofed animals. *Ann. N. Y. Acad. Sci.* **22**, 267-326.

Hildebrand, M. (1974). *Analysis of Vertebrate Structure.* New York: John Wiley & Sons.

Hoerner, S. F. (1965). *Fluid-Dynamic Drag.* Brick Town, NJ: Hoerner Fluid Dynamics.

Holzman, R., Day, S. W., Mehta, R. S. and Wainwright, P. C. (2008). Jaw protrusion enhances forces exerted on prey by suction feeding fishes. *J. R. Soc. Interface* **5**, 1445-1457.

Kier, W. M. and Smith, K. K. (1985). Tongues, tentacles and trunks: the biomechanics of movement in muscular hydrostats. *Zool. J. Linn. Soc.* **83**, 307-324.

Lappin, A. K., Monroy, J. A., Pilarski, J. Q., Zepnewski, E. D., Pierotti, D. J. and Nishikawa, K. C. (2006). Storage and recovery of elastic potential energy powers ballistic prey capture in toads. *J. Exp. Biol.* **209**, 2535-2553.

McHenry, M. J. (2011). There is no trade-off between force and velocity in a dynamic lever system. *Biol. Lett.* **7**, 384-386.

McNeill, P., Hoyle, G. and Burrows, M. (1972). Fine structures of the muscles controlling the strike of the mantis shrimp, *Hemisquilla. J. Exp. Zool.* **179**, 395-416.

Meriam, J. L. and Kraige, L. G. (1997). *Dynamics.* New York: John Wiley & Sons, Inc.

Muller, M. (1987). Optimization principles applied to the mechanism of neurocranium levation and mouth bottom depression in bony fishes (*Halecostomi*). *J. Theor. Biol.* **126**, 343-368.

Patek, S. and Caldwell, R. (2005). Extreme impact and cavitation forces of a biological hammer: strike forces of the peacock mantis shrimp *Odontodactylus scyllarus. J. Exp. Biol.* **208**, 3655-3664.

Patek, S. N., Korff, W. L. and Caldwell, R. L. (2004). Biomechanics: deadly strike mechanism of a mantis shrimp. *Nature* **428**, 819-820.

Patek, S. N., Nowroozi, B. N., Baio, J. E., Caldwell, R. L. and Summers, A. P. (2007). Linkage mechanics and power amplification of the mantis shrimp's strike. *J. Exp. Biol.* **210**, 3677-3688.

Paul, B. (1979). *Kinematics and Dynamics of Planar Machinery.* Englewood Cliffs, NJ: Prentice Hall.

Rayner, J. M. V. (1985). Linear relations in biomechanics-the statistics of scaling functions. *J. Zool.* **206**, 415-439.

Richards, C. T. (2011). Building a robotic link between muscle dynamics and hydrodynamics. *J. Exp. Biol.* **214**, 2381-2389.

Rohlf, F. J. (2005). *TpsDig2, Digitize Landmarks and Outlines v2.10.* Stony Brook, NY: Department of Ecology and Evolution, State University of New York at Stony Brook.

Sakamoto, M. (2010). Jaw biomechanics and the evolution of biting performance in theropod dinosaurs. *Proc. R. Soc. Lond. B* **277**, 3327-3333.

Sarpkaya, T. (1986). Force on a circular cylinder in viscous oscillatory flow at low Keulegan-Carpenter numbers. *J. Fluid Mech.* **165**, 61-71.

Seeram, E. (2000). *Computed Tomography: Physical Principles, Clinical Applications, and Quality Control.* Philadelphia, PA: Saunders.

Smith, J. M. and Savage, R. J. G. (1956). Some locomotory adaptations in mammals. *J. Linn. Soc. Lond. Zool.* **42**, 603-622.

Sokal, R. R. and Rohlf, F. J. (1995). *Biometry.* New York: W. H. Freeman and Company.

Wainwright, P., Bellwood, D., Westneat, M., Grubich, J. and Hoey, A. (2004). A functional morphospace for the skull of labrid fishes: patterns of diversity in a complex biomechanical system. *Biol. J. Linn. Soc.* **82**, 1-25.

Westneat, M. W. (1995). Feeding, function, and phylogeny: analysis of historical biomechanics in labrid fishes using comparative methods. *Syst. Biol.* **44**, 361-383.

Zack, T. I., Claverie, T. and Patek, S. N. (2009). Elastic energy storage in the mantis shrimp's fast predatory strike. *J. Exp. Biol.* **212**, 4002-4009.

Zajac, F. (1993). Muscle coordination of movement: a perspective. *J. Biomech.* **26**, 109-124.